

Rethinking domain generalization in medical image segmentation: One image as one domain

Jin Hong^{1,*}, Bo Liu², Guoli Long¹

1. School of Information Engineering, Nanchang University, Nanchang, 330031, China

2. School of Mathematics and Computer Science, Nanchang University, Nanchang, 330031, China

E-mail: hongjin@ncu.edu.cn; liuboncu@email.ncu.edu.cn; 6003122121@email.ncu.edu.cn;

* Correspondence should be addressed to Jin Hong

Abstract: Domain shifts in medical image segmentation, particularly when data comes from different centers, pose significant challenges. Intra-center variability, such as differences in scanner models or imaging protocols, can cause domain shifts as large as, or even larger than, those between centers. To address this, we propose the "one image as one domain" (OIOD) hypothesis, which treats each image as a unique domain, enabling flexible and robust domain generalization. Based on this hypothesis, we develop a unified disentanglement-based domain generalization (UniDDG) framework, which simultaneously handles both multi-source and single-source domain generalization without requiring explicit domain labels. This approach simplifies training with a fixed architecture, independent of the number of source domains, reducing complexity and enhancing scalability. We decouple each input image into content representation and style code, then exchange and combine these within the batch for segmentation, reconstruction, and further disentanglement. By maintaining distinct style codes for each image, our model ensures thorough decoupling of content representations and style codes, improving domain invariance of the content representations. Additionally, we enhance generalization with expansion mask attention (EMA) for boundary preservation and style augmentation (SA) to simulate diverse image styles, improving robustness to domain shifts. Extensive experiments show that our method achieves Dice scores of 84.43% and 88.91% for multi-source to single-center and single-center generalization in optic disc and optic cup segmentation, respectively, and 86.96% and 88.56% for prostate segmentation, outperforming current state-of-the-art domain generalization methods, offering superior performance and adaptability across clinical settings.

Keywords: Domain generalization; Medical image segmentation; Single-center and multi-center variability; Disentanglement-based framework; One image as one domain (OIOD)

1. Introduction

Deep learning has significantly advanced the field of medical image segmentation, enabling automated and highly accurate delineation of anatomical structures across various imaging modalities. Notable breakthroughs, such as U-Net [1] and its derivatives, have become foundational architectures for tasks like organ segmentation, tumor detection, and other critical medical applications [2, 3]. These models, however, typically rely on a key assumption: that the training data and test data share the same underlying distribution. This assumption, known as the independent and identically distributed (i.i.d.) hypothesis, has underpinned much of the success in medical image segmentation. In reality, however, training data and test data often come from different distributions, leading to a domain shift that negatively impacts model performance when deployed in clinical practice [4-6]. As a result, models that perform well on training datasets may struggle to achieve the same level of accuracy on new, unseen

data, underscoring the need to address domain shift in medical image segmentation [7].

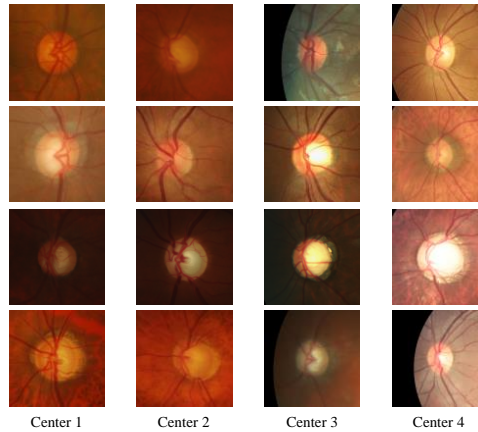


Figure 1 Illustration of image differences between centers and within centers.

To address the issue of reduced performance in trained networks across different domains, researchers have explored a range of strategies for medical image analysis. A commonly adopted approach is transfer learning, particularly through fine-tuning, which adjusts network weights to accommodate the unique characteristics of a new domain. However, fine-tuning typically requires additional labeled data from the target domain, presenting challenges due to the high cost and effort needed for medical image annotation. In response, various unsupervised domain adaptation techniques have been developed to reduce the distribution gap between source and target domains without requiring labels from the latter. This approach has proven effective in medical image segmentation by facilitating knowledge transfer across domains [8]. However, despite its effectiveness, DA faces several significant challenges. First, DA typically requires access to the target domain data during training, which is not always available in real-world scenarios due to privacy concerns, lack of labeled data, or the infeasibility of obtaining data from future unseen domains [9]. Second, DA methods often lead to catastrophic forgetting, where the model’s performance on the source domain deteriorates after adapting to a new target domain [10]. This phenomenon is particularly problematic in healthcare settings, where a model must maintain high performance across all domains, including the original source domain.

Domain generalization (DG) methods, on the other hand, address those challenges by enhancing a model’s ability to generalize to unseen domains without requiring access to target domain data during training and without catastrophic forgetting [11]. While DG techniques have successfully reduced the performance gap between source and target domains in natural image classification, their application to medical image segmentation presents unique challenges due to the complex and structured prediction nature of segmentation tasks. In medical imaging, CNN-based methods have explored data augmentation to improve generalization; however, they typically rely on single-source domain training, which limits their ability to capture the intricate relationships between multiple domains that could enhance model performance on previously unseen target data [12].

To address these limitations, recent DG methods have taken two primary directions: image-based and feature-based approaches. Image-based DG methods, such as BigAug, apply extensive data augmentation by stacking transformations to mimic domain shifts, aiming to bridge the domain gap through simulation [13]. However, the effectiveness of these augmentations often depends on data-specific configurations, which limits their generalizability across diverse medical imaging environments.

Feature-based DG methods, by contrast, emphasize learning domain-invariant representations to capture core features that remain consistent across domains. Domain-oriented feature embedding, for example, uses knowledge from multi-site datasets to make semantic features more domain-discriminative [9], while techniques like Domain Composition and Attention Network (DCA-Net) use a representation bank and attention modules to dynamically adapt features based on domain context [14]. Although these methods benefit from domain-specific knowledge pools, their reliance on predefined representation banks restricts generalization across a broader range of domains.

In recent developments, feature disentanglement has been explored to separate domain-invariant content from domain-specific styles, which enables models to learn flexible representations across modalities. However, traditional GAN-based disentanglement methods often require multiple encoders and discriminators for each known domain, resulting in a complex training process and limited scalability to unseen domains. A CDDSA framework addresses these limitations with introducing a contrastive learning approach that disentangles domain-invariant content while augmenting style representations to increase model adaptability [10]. By reducing dependence on complex GAN architectures and extensive domain-specific encoders, CDDSA enhances scalability and allows for improved generalization to unseen domains, marking a significant step forward in the robustness of medical image segmentation across diverse clinical settings.

Although these methods are very promising, they often treat different centers as different domains when facing multi center scenarios in the source domain, ignoring the fact that significant domain changes may occur within one center. In some cases—particularly after observing various multi-center datasets—the variability within a center, due to different scanner models or imaging protocols, may result in domain shifts even greater than those observed between centers. As shown in Figure 1, there are significant differences in the images within each center, and in some cases, images from different centers may exhibit similarities. *This phenomenon makes it unreliable to classify images from a single center into one domain and to categorize images from different centers into distinct domains.* Based on this, we believe that rethinking the current domain partitioning scheme is highly necessary to improve the model's generalization ability.

Ideally, we need to meticulously verify the instrument parameters for each image at the time of acquisition to ensure that images scanned under identical conditions are classified into the same domain. We refer to this process as domain identification. Domain identification, however, is a complex and labor-intensive task, often requiring detailed knowledge of the scanner model, scanning parameters, and other factors for each image. In some cases, the detailed information of these images may be lost, complicating the identification process even further.

In this paper, we propose a novel perspective on domain generalization by redefining the concept of a domain. Instead of grouping images based on scanner or center characteristics, we treat each image as a unique domain, under the assumption that every image exhibits its own domain shift and style variation. This approach, which we refer to as the "one image as one domain" (OIOD) hypothesis, redefines the concept of domain partitioning in medical image segmentation. It allows for more flexible and robust generalization across diverse domains, whether they are from a single source or multiple sources. Building on this assumption, we develop a unified disentanglement-based domain generalization (UniDDG) framework for medical image segmentation that can flexibly accommodate scenarios involving both single-source and multiple-source domains. This framework enhances generalization across diverse unseen domains without requiring explicit domain labels. Additionally, it maintains a fixed computational complexity and workload that does not increase with the number of source domains,

and its non-reliance on GANs simplifies the training process. The contributions of our work are summarized as follows:

(i) To the best of our knowledge, we are the first to redefine the concept of a domain by treating each image as a unique domain, addressing the inherent variability within and across centers. This novel perspective, named as the "one image as one domain" (OIOD) hypothesis, eliminates the reliance on explicit domain labels and improves the model's adaptability to diverse unseen domains.

(ii) We propose the UniDDG framework, a unified disentanglement-based approach for domain generalization that accommodates both single-source and multi-source scenarios, ensuring consistent computational complexity and scalability regardless of the number of source domains.

(iii) We introduce expansion mask attention (EMA), which applies an expansion mask during reconstruction to focus on target regions and their surroundings, enhancing boundary preservation and improving segmentation accuracy.

(iv) We develop style augmentation (SA), which generates random style codes to simulate diverse image styles, increasing the model's robustness to domain variations and enhancing its generalization capability.

(v) Extensive experiments on two segmentation tasks—optic disc and optic cup segmentation, as well as prostate segmentation—demonstrate the superior performance and adaptability of our proposed framework compared to state-of-the-art methods.

2. Related work

2.1. Domain adaptation for image segmentation

Domain adaptation (DA) has become a pivotal approach to address the domain shift problem in medical image segmentation, particularly when training and test data come from different distributions. Traditional methods in DA, such as fine-tuning pre-trained networks on new domain data, aim to minimize the distribution gap between the source and target domains. However, this often requires labeled data from the target domain, which can be difficult and costly to obtain in medical contexts. To address this, unsupervised domain adaptation (UDA) has been proposed, where the model learns to adapt to the target domain without requiring any labeled data. Various unsupervised domain adaptation techniques have been proposed to address cross-domain discrepancies. These include feature-level alignment [15-23], pixel-level alignment [24-27], self-learning approaches [28-31], as well as hybrid methods that combine these strategies [4, 8, 32, 33].

Current research is limited to two domains (a source domain and a target domain), failing to fully leverage labeled data from many other centers. In the field of image segmentation, two representative works have demonstrated the advantages of multi-source unsupervised domain adaptation over single-source methods when dealing with multi-centered source domain data [34, 35]. Segmentation accuracy in multi-source domains is significantly higher than in single-source domains. Zhao et al. [34] combined pixel-level alignment with feature distribution alignment, using GANs to transform two source domain images into target domain style images, which are then merged into a single source domain. They applied adversarial learning to implicitly align feature distributions between the source and target domains. When extending this method to more source domains, the number of adversarial training iterations must increase accordingly. Overuse of adversarial training not only increases model complexity but may also prevent the model from converging to a Nash equilibrium [36, 37]. He et al. [35] integrated pixel-level alignment with self-supervised learning, converting RGB images into LAB color space, and explicitly

shifting pixel distributions to transform source domain images into the target domain style. They further improved model performance by using feature distribution differences or pseudo-labels from two model outputs in a mutual learning framework. The number of segmentation networks in this framework equals the number of source domains, and when scaled to more source domains, substantial computational resources are required, particularly for three-dimensional image inputs.

2.2. Domain generalization for image segmentation

While domain adaptation (DA) aims to adapt a model to a target domain using data from that domain, it requires access to target domain data during training and may lead to catastrophic forgetting of the source domain. To overcome these challenges, domain generalization (DG) techniques have emerged as a promising alternative. Domain generalization focuses on enhancing a model's ability to generalize to unseen domains without the need for target domain data during training or risking performance degradation on the source domain. In the context of image segmentation, DG aims to improve model robustness across various domains, including unseen domains, by leveraging data augmentation and other strategies.

The first direction in DG for image segmentation is related to data augmentation, such as Manifold Mixup [38] and CutMix [39], which create new training samples by interpolating or mixing images in the feature space. These methods have proven effective in generating domain-invariant representations, enhancing model robustness in unseen environments. Zhang et al. [13] explored the idea of deep stacked transformations (BigAug) to generalize deep learning models for medical image segmentation, using transformations that simulate domain shifts to improve model generalization to unseen datasets. Such approaches rely heavily on the premise that augmentations can simulate diverse variations in data, making them effective for improving model adaptability to new domains without requiring labeled data from those domains.

Another line of work focuses on semantic-aware domain generalization, which tries to improve segmentation by leveraging semantic information to guide the model's ability to generalize. Peng et al. [40] proposed a semantic-aware domain generalized segmentation approach that learns robust representations across different domains, ensuring that the model's predictions remain consistent even in the presence of domain shifts. Other approaches, such as those proposed by Choi et al. [41], enhance model robustness in segmentation tasks by introducing selective whitening to reduce domain-specific variations, achieving improved performance on unseen domains. However, many of these methods still rely on single-source domain data and fail to fully leverage multi-source domain data, which could provide more comprehensive insights into the generalization process.

When extending DG techniques to multi-source domains, new challenges arise. Methods such as Dofe [9], which focuses on domain-oriented feature embedding for generalizable fundus image segmentation, and Domain and Content Adaptive Convolution (D-CAC) [42], which adapts convolutional layers to handle multi-source domains, address these complexities by learning domain-invariant features while maintaining adaptability to diverse data distributions. Additionally, Federated Domain Generalization (Feddg) [43] has explored federated learning techniques to address domain variability across multiple sources. Despite these advancements, existing methods often still suffer from limitations, such as the need for explicit domain identification, the scalability issues when the number of source domains increases, and the increased training difficulty due to the use of multiple GANs.

To address these challenges, we propose a novel approach based on style and content disentanglement, as explored in the CDDSA framework [10]. Our proposed method directly addresses

the challenges faced by traditional domain generalization approaches. By treating each image as a unique domain, we eliminate the need for explicit domain labels, making it applicable to both single-source and multi-source domain generalization scenarios. Importantly, our method maintains a fixed computational complexity, regardless of the number of source domains. This is achieved by using a streamlined architecture consisting of only one content encoder, one style encoder, a segmentation network head, and a decoder. Unlike previous methods that rely on multiple models or complex GAN architectures, our approach reduces the training difficulty and computational overhead, making it more scalable and efficient. The lack of GANs in our framework simplifies training, allowing for faster convergence and less resource-intensive computation.

3. Method

3.1. The unified disentanglement-based domain generalization framework

Multi-center-based domain generalization for medical image segmentation is generally defined as enhancing the ability of a segmenter S , trained on datasets $\{D_1, \dots, D_K\}$ from K labeled centers, to generalize effectively to an additional dataset D_{K+1} from an unobserved target center. However, this paper introduces a novel perspective on domain partitioning, treating each image as an individual domain with its own distinct style, even if images come from the same center. As a result, data from multiple source centers can be mixed together without the need to classify images by center-based domains. Specifically, the training data is represented as $\{x_1, \dots, x_t\}$, where x denotes an individual image, and t represents the total number of images across all source domains.

The proposed unified disentanglement-based domain generalization (UniDDG) framework is illustrated in Figure 2. All source domain images are mixed in a single data pool, and during each batch processing, a batch of n images $\{x_1, \dots, x_n\}$ is randomly sampled from this pool. This batch of images is then fed into a content encoder E_{con} and a style encoder E_{sty} to perform feature disentanglement, resulting in corresponding content representations $\{c_1, \dots, c_n\}$ and style codes $\{s_1, \dots, s_n\}$. Subsequent operations involve exchanging and combining the content representations and style codes within the batch for segmentation, reconstruction, and further disentanglement. This process is grounded in the assumption that each image possesses a unique style, as stated in the OIOD hypothesis. By decoupling each image into its content representation and style code, the model ensures that the style codes for different images are distinct, effectively isolating domain-specific variations in the style codes. This enables the model to learn the unique style of each image while maintaining the content representation as domain-invariant, leading to a more thorough disentanglement of content and style. Additionally, by randomly generating new style codes for each content representation, the diversity of styles can be enhanced and the model’s ability to disentangle content from style variations can also be improved. The following steps outline how the content representations and style codes are utilized:

- (i) The obtained content representations $\{c_1, \dots, c_n\}$ are input into a segmenter S to obtain predicted segmentation results $\{y'_1, \dots, y'_n\}$. By calculating the discrepancy between these predictions and the ground truth $\{y_1, \dots, y_n\}$, the segmentation loss \mathcal{L}_{seg} is obtained.

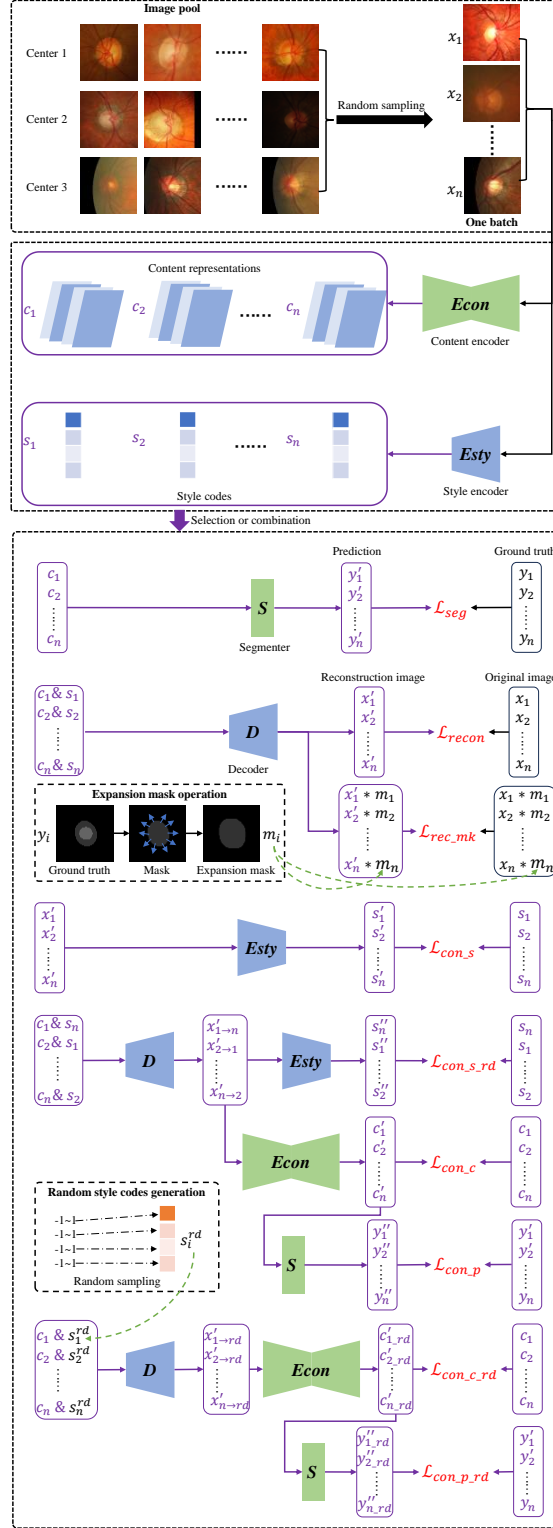


Figure 2 (Best viewed in color) Overview of the proposed unified disentanglement-based domain generalization framework.

(ii) The content representations $\{c_1, \dots, c_n\}$ and style codes $\{s_1, \dots, s_n\}$ are paired and input into a decoder D to reconstruct the original images $\{x'_1, \dots, x'_n\}$. By calculating the discrepancy between the reconstructed images and the originals $\{x_1, \dots, x_n\}$, the reconstruction loss \mathcal{L}_{recon} is derived. To focus D more on the segmentation region and its surrounding areas during reconstruction, an expansion mask is introduced. Specifically, the ground truth y_i is converted into a binary mask, and the boundary of the

target area in the mask is expanded outward by a certain distance to generate the expansion mask m_i . This mask is then multiplied with both the reconstructed and original images to calculate their discrepancy, yielding the masked reconstruction loss \mathcal{L}_{re_mk} .

(iii) The reconstructed images $\{x'_1, \dots, x'_n\}$ are re-disentangled by inputting them into *Esty* to extract new style codes $\{s'_1, \dots, s'_n\}$. The discrepancy between these new codes and the original style codes $\{s_1, \dots, s_n\}$ is used to define the style consistency loss \mathcal{L}_{con_s} .

(iv) The content representations $\{c_1, \dots, c_n\}$ and style codes $\{s_1, \dots, s_n\}$ are randomly paired and input into *D* to generate reconstructed images with exchanged styles $\{x'_{1 \rightarrow n}, \dots, x'_{n \rightarrow 2}\}$. These reconstructed images, in which the styles have been swapped, are then passed through *Econ* and *Esty* to re-disentangle them, obtaining content representations $\{c'_1, \dots, c'_n\}$ and style codes $\{s''_1, \dots, s''_n\}$. By calculating the discrepancy between these representations and the content representations $\{c_1, \dots, c_n\}$ and style codes $\{s_1, \dots, s_n\}$, content and style consistency losses \mathcal{L}_{con_c} and $\mathcal{L}_{con_s_rd}$ are obtained. The content representations $\{c'_1, \dots, c'_n\}$ are also fed into *S* to get segmentation predictions $\{y''_1, \dots, y''_n\}$. By calculating the difference between these predictions and the initial segmentation results $\{y'_1, \dots, y'_n\}$, the segmentation consistency loss \mathcal{L}_{con_p} is derived.

(v) To enhance the robustness of the segmenter and content encoder against variations in image styles, additional styles s_i^{rd} are randomly generated named style augmentation. These new style codes are combined with the initial content representations $\{c_1, \dots, c_n\}$ and input into *D* to produce randomly styled reconstructed images $\{x'_{1 \rightarrow rd}, \dots, x'_{n \rightarrow rd}\}$. These reconstructions are then input into *Econ* to obtain content representations $\{c'_{1 \rightarrow rd}, \dots, c'_{n \rightarrow rd}\}$. The discrepancy between these representations and the initial content representations yields the content consistency loss $\mathcal{L}_{con_c_rd}$. Furthermore, $\{c'_{1 \rightarrow rd}, \dots, c'_{n \rightarrow rd}\}$ is also input into *S*, generating predicted segmentation results $\{y''_{1 \rightarrow rd}, \dots, y''_{n \rightarrow rd}\}$. By calculating the discrepancy between these predictions and the initial segmentation results $\{y'_1, \dots, y'_n\}$, the segmentation consistency loss $\mathcal{L}_{con_p_rd}$ is obtained.

3.2. Content encoder and segmenter

We use a modified U-Net [1] as the backbone to implement *Econ*, adjusting the final layer's output channel to R and using tanh activation. For input image x_i with height H and width W , the output $c_i \in [-1, 1]^{H \times W \times R}$ is structured so each channel captures specific anatomical details. Unlike SDNet [44], which restricts c_i to binary values, our approach uses tanh activation $\tanh(x) = \frac{e^x - e^{-x}}{e^x + e^{-x}}$ to retain detailed structures, enhancing image reconstruction and style augmentation. The anatomical representation extraction is:

$$c_i = E_{con}(x_i) \quad (1)$$

This representation c_i is input to a segmentation network *S*, shown as in Figure 3, producing a probability map $y'_i = S(c_i)$. Let y_i denotes the ground truth, the segmenter *S* is optimized by minimizing the segmentation loss \mathcal{L}_{seg} between y'_i and y_i . Dice coefficient is employed as the segmentation loss in this study [45]:

$$\mathcal{L}_{seg} = \frac{\sum_{i=1}^N 2y_i y'_i}{\sum_{i=1}^N y_i y_i + \sum_{i=1}^N y'_i y'_i} \quad (2)$$

where N represents the number of the inputs.

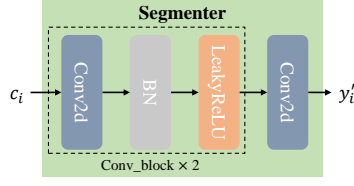


Figure 3 (Best viewed in color) Structure of the segmentation network.

3.3. Style encoder

In our approach, the domain-specific modality representations are generated by a style encoder *Esty*, implemented as the encoder part of a Variational Autoencoder (VAE) [46], as shown in Figure 4. The VAE typically learns a low-dimensional latent space where the learned latent representations approximate an isotropic multivariate Gaussian distribution $p(\mathbf{z}) = \mathcal{N}(0,1)$. For each input x_i , *Esty* predicts the mean μ_i and variance σ_i of the latent distribution $\mathbf{z} \in \mathbb{R}^{1 \times Z}$, where Z is the length of the latent code. The style code s_i for an input image x_i is then sampled from the predicted distribution defined by the mean μ_i and variance σ_i .

Specifically, we omit the *KL* divergence loss that would usually be computed between the estimated Gaussian distribution $q(\mathbf{z} | \mu_i, \sigma_i)$ and the unit Gaussian $p(\mathbf{z})$. Including *KL* divergence tends to result in nearly identical style codes for each image within a batch, which conflicts with our assumption that each image has a distinct style code. By excluding the *KL* divergence, we allow more variability in the style representation, aligning with our goal of capturing unique style characteristics for each image.

Thus, once training is complete, sampling from the latent space without *KL* regularization provides distinct style codes. These are then paired with content representations and passed to the decoder, which acts as a generative model to reconstruct images, as detailed in the following sections.

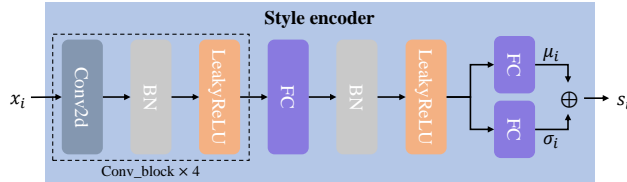


Figure 4 (Best viewed in color) Structure of the style encoder.

3.4. Decoder

In this study, we adopt the same reconstruction decoder D structure as in reference [10]. Figure 5 presents the architecture of D , which produces a reconstructed image x'_i by combining two separate representations, c_i for content and s_i for style. These two representations collaborate in a "repainting" role: c_i defines the structural details, while s_i supplies stylistic features across the image [47].

To generate the final image, the decoder processes c_i through three repainting blocks for style adjustments and one convolution layer. In each repainting block, the adaptive scaling α and bias β parameters that are used in Adaptive Instance Normalization (AdaIN) can be predicted with the guidance of the style code s_i . Specifically, AdaIN individually transforms each channel of the feature map outputted by the previous convolution layer in each repainting block, adjusting style through calculated α and β values for every channel.

The decoder thus progressively layers style information over the content structure, adapting from coarse to refined details. The final output image x'_i can be expressed as:

$$x'_i = D(c_i, s_i) \quad (3)$$

Because c_i and s_i originate from x_i , the reconstructed image x'_i should approximate the original input as closely as possible. To achieve this, we apply a reconstruction loss based on $L1$ loss function for its robustness to outliers:

$$\mathcal{L}_{recon} = \frac{1}{N} \sum_{i=1}^N |x'_i - x_i| \quad (4)$$

where N represents the number of the inputs.

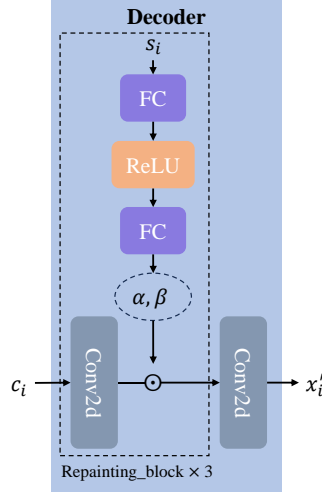


Figure 5 (Best viewed in color) Structure of the reconstruction decoder.

3.5. Expansion mask attention for reconstruction

In the previous section, the reconstruction loss was computed based on the difference between the entire reconstructed image and the original, controlling the overall quality of the image restoration. Since it is challenging for the decoder to perfectly reconstruct an image identical to the original (i.e., the reconstruction loss cannot be zero), we want the model to focus more on the target segmentation area and its surrounding regions. This is because the primary objective of segmentation is to identify the boundaries of the target object, and for accurate reconstruction, the boundaries must be precisely captured. As a result, the reconstruction should emphasize not only the segmented target area but also its surrounding context. To guide this process, we introduced expansion mask attention (EMA), which specifies the region where more precise reconstruction is needed, ensuring the model prioritizes accurate restoration in these key areas.

The process of obtaining the expansion mask is illustrated in Figure 2. First, the ground truth mask is binarized, with pixel values set to 0 for the background and 1 for the target object. The target region (pixels with a value of 1) is then dilated, slightly extending the mask beyond the object boundary. The expansion mask m_i is subsequently applied to both the reconstructed and original images via element-wise multiplication, and a reconstruction loss \mathcal{L}_{rec_mk} is calculated between the two, $x'_i * m_i$ and $x_i * m_i$. This process directs the decoder to focus on the regions covered by the expansion mask, thereby enhancing the preservation of boundary details between the segmented object and the surrounding background. The masked reconstruction loss \mathcal{L}_{rec_mk} which is based on based on $L1$ loss can be defined as:

$$\mathcal{L}_{rec_mk} = \frac{1}{N} \sum_{i=1}^N |x'_i * m_i - x_i * m_i| \quad (5)$$

3.6. Style augmentation

To enhance the robustness of the content encoder and segmenter against image style variations, we adopt a style augmentation (SA) approach. As shown in Figure 2, we first generate random style code by sampling each element from a uniform distribution in the range of -1 to 1. This random style code s_i^{rd} is then combined with the content representation c_i obtained from the initial decoupling and fed into the decoder D to produce a style-augmented reconstruction image $x'_{i \rightarrow rd}$. This image is subsequently passed through the content encoder E_{con} , and the resulting content representation $c'_{i \rightarrow rd}$ is constrained to match the original content representation c_i via a consistency loss $\mathcal{L}_{con_c_rd}$. $c'_{i \rightarrow rd}$ is then input into the segmenter, where the predicted segmentation output $y''_{i \rightarrow rd}$ is required to align with the original segmentation result y'_i , again governed by a consistency loss $\mathcal{L}_{con_p_rd}$. The above two consistency losses are based on based on L1 loss:

$$\mathcal{L}_{con_c_rd} = \frac{1}{N} \sum_{i=1}^N |c'_{i \rightarrow rd} - c_i| \quad (6)$$

$$\mathcal{L}_{con_p_rd} = \frac{1}{N} \sum_{i=1}^N |y''_{i \rightarrow rd} - y'_i| \quad (7)$$

3.7. Overall loss function

The UniDDG framework incorporates a total of nine loss functions. Five of these are defined in previous sections, while the remaining four— \mathcal{L}_{con_s} , \mathcal{L}_{con_c} , $\mathcal{L}_{con_s_rd}$, and \mathcal{L}_{con_p} —are consistency loss functions based on L1 loss, and thus their detailed formulations are omitted for brevity. The overall loss function of the UniDDG framework is as follows:

$$\begin{aligned} \mathcal{L}_{all} = & \lambda_1 \mathcal{L}_{seg} + \lambda_2 \mathcal{L}_{recon} + \lambda_3 \mathcal{L}_{rec_{mk}} + \lambda_4 \mathcal{L}_{con_s} + \lambda_5 \mathcal{L}_{con_{s_rd}} \\ & + \lambda_6 \mathcal{L}_{con_c} + \lambda_7 \mathcal{L}_{con_p} + \lambda_8 \mathcal{L}_{con_{c_rd}} + \lambda_9 \mathcal{L}_{con_{p_rd}} \end{aligned} \quad (8)$$

where $\lambda_1, \dots, \lambda_9$ act as trade-off parameters for different loss terms.

4. Experiment results and discussion

4.1. Datasets

In this study, we adopted two types of public challenge datasets for evaluating the proposed UniDDG framework: a multi-center retinal fundus image dataset¹ [48-50] and a multi-center prostate T2-weighted MRI dataset [51-53].

Multi-center retinal fundus image dataset: We evaluated our approach for Optic Cup (OC) and Optic Disc (OD) segmentation using a publicly available multi-center retinal fundus image dataset. This dataset consists of images from four different public fundus image collections, each captured with different scanners at various sites, resulting in distinct domain discrepancies in visual appearance and image quality. Specifically:

- a) Center 1 is from the Drishti-GS dataset [48], with 50 images for training and 51 for testing.
- b) Center 2 is from the RIM-ONE-r3 dataset [49], containing 99 images for training and 60 for testing.
- c) Center 3 and 4 are from the REFUGE challenge [50], with 320 training images and 80 testing images from the training and validation datasets, respectively.

A summary of the statistics for these multi-center retinal fundus images is presented in Table 1.

¹ <https://github.com/emma-sjwang/Dofe>

Table 1 Overview of the retinal fundus image statistics across the four centers used in our experiment.

Task	Center No.	Dataset	Images (train / test)	Scanners
OC/OD segmentation	Center 1	Drishti-GS [48]	50 / 51	Aravind eye hospital
	Center 2	RIM-ONE-r3 [49]	99 / 60	Nidek AFC-210
	Center 3	REFUGE [50] (train)	320 / 80	Zeiss Visucam 500
	Center 4	REFUGE [50] (val)	320 / 80	Canon CR-2

In this study, it is important to note that the segmentation of the OD refers specifically to the segmentation of the OD region excluding the OC, as the OD anatomically encompasses the OC.

Multi-center prostate T2-weighted MRI dataset: We also evaluated our approach for prostate segmentation using a publicly available multi-center prostate T2-weighted MRI dataset. This dataset consists of images from five different public fundus image collections, each captured with different distributions at various sites, resulting in distinct domain discrepancies in visual appearance and image quality. Specifically:

- a) Center 1 and center 2 are from the NCI-ISBI13 dataset [51], and both centers contain 30 cases.
- b) Center 3 is from the I2CVB dataset [52], including 19 cases.
- c) Center 4 and center 5 are from the PROMISE12 dataset [53], with center 4 containing 12 cases and center 5 containing 13 cases.

For each of the five center datasets, we randomly divided the original site dataset into training and testing sets with a 4:1 ratio. A summary of the statistics for these multi-center prostate T2-weighted MRI cases is presented in Table 2.

Table 2 Overview of the prostate T2-weighted MRI case statistics across the five centers used in our experiment.

Task	Center No.	Dataset	Cases (train / test)	Field strength (T)	Resolution (in/through plane) (mm)	Coil
Prostate segmentation	Center 1	NCI-ISBI13 [51]	24 / 6	3	0.6-0.625 / 3.6-4	Surface
	Center 2	NCI-ISBI13 [51]	24 / 6	1.5	0.4 / 3.0	Endorectal
	Center 3	I2CVB [52]	15 / 4	3	0.67-0.79 / 1.25	-
	Center 4	PROMISE12 [53]	9 / 3	1.5	0.625 / 3.6	Endorectal
	Center 5	PROMISE12 [53]	10 / 3	1.5 and 3	0.325-0.625 / 3-3.6	-

For preprocessing, we applied basic data augmentation (BDA) techniques (random flip, random rotate, random scale, random shift, random noise, random brightness, and random channel swap) to enhance the diversity of the training samples. During training, the retinal fundus images were randomly cropped to a size of 256×256 , and the prostate MRI slices were resized to 256×256 . Note that fundus images are three-channel color images, while prostate MRI slices are single-channel grayscale images. To adapt the prostate MRI slices to the framework of this study, we replicated the single channel to convert them into three-channel images. Note that all background slices of prostate MRI datasets have been removed.

We assess the effectiveness of our proposed method from two perspectives: *first, the generalization from multiple source centers to a single target center; and second, the performance within a single center.* To evaluate the generalizability of the UniDDG framework across multiple source centers to a single target center, we employed a leave-one-center-out cross-validation strategy, where one center is held out for testing while the remaining centers are used for training. It is important to highlight that only the training image/slice sets from the multi-source centers are used for network training, while the testing image/slice sets from the target center are employed to assess the network's performance. Furthermore, we also evaluate the generalization ability of our method within a single center, where both the training and testing datasets are derived from the same center.

4.2. Implementation details

Training and inference were carried out on a single NVIDIA GeForce RTX 2080 Ti GPU. The content encoder *Econ* was constructed using a U-Net [1] as the core architecture, with progressively increasing channel sizes of 16, 32, 64, 128, and 256 across five resolution scales. The number of channels for the content representations was fixed at $R = 8$. The segmenter *S* consists of two convolutional blocks: the first block includes a 3×3 convolution followed by batch normalization (BN) and LeakyReLU (with a slope of 0.2), while the second block features a 1×1 convolution followed by a Softmax layer to output a segmentation probability map. The style encoder *Esty* contains convolutional layers with down-sampling steps to reduce spatial resolution, and its final output is passed through two fully connected layers to produce the mean and variance for the latent style code, with the size set to $Z = 48$.

The loss function weights were set as follows: $\lambda_1=5.0$, $\lambda_2=5.0$, $\lambda_3=10.0$, $\lambda_4=1.0$, $\lambda_5=5.0$, $\lambda_6=1.0$, $\lambda_7=1.0$, $\lambda_8=1.0$, $\lambda_9=1.0$. The models were optimized using the RMSprop optimizer, with an initial learning rate of 10^{-4} . For each mini-batch, the number of images/slices was set as 8. The number of epochs was set as 500. Segmentation performance was evaluated using two metrics: the Dice coefficient (Dice) and the Average Symmetric Surface Distance (ASSD).

4.3. Retinal fundus image segmentation

4.3.1. Generalization from multiple source centers to a single target center

(i) Comparison with state-of-the-art DG methods: For evaluating the generalization performance of the proposed UniDDG framework from multiple source centers to a single target center, a leave-one-center-out cross-validation strategy is employed. Initially, we treated all available training centers as a unified dataset, disregarding domain shifts within the training set, and trained a U-Net [1] using standard Dice loss. This model was then directly applied to an unseen center, serving as the experiment's lower bound. Conversely, for each center, we conducted training and testing exclusively within its dataset, ensuring no unseen centers were involved. This setup establishes the upper bound for DG. Additionally, to provide more granular benchmarks, we excluded basic data augmentation (BDA) operations from both setups. This led to the establishment of upper bound w/o BDA and lower bound w/o BDA as additional references, offering a clearer understanding of the impact of domain shifts and the benefits introduced by data augmentation. To evaluate DG performance, we benchmarked our proposed UniDDG against five cutting-edge methods: Cutmix [39], Mixup [54], BigAug [13], Manifold Mixup [38], Dofe [9], and CDDSA [10]. These methods represent various strategies for enhancing domain generalization, including CutMix [39] and Mixup [54], which generate augmented samples by blending images, BigAug [13], which stacks diverse transformations to mimic domain shifts, Manifold Mixup [38], which interpolates in the feature space to create domain-invariant representations, Dofe [9], which employs domain-oriented feature embedding for robust segmentation across multiple domains, and CDDSA [10], which leverages contrastive domain disentanglement and style augmentation to enhance generalization. Note all DG methods, including UniDDG, are performed with BDA.

Table 3 Evaluation of Dice Scores (%) using diverse DG approaches on fundus image dataset from multiple source centers to a single target center

Method	Center1		Center2		Center3		Center4		Average		
	OC	OD	OC	OD	OC	OD	OC	OD	OC	OD	All
Lower bound w/o BDA	76.55	74.06	67.91	64.35	81.10	84.28	77.89	69.29	75.86	73.00	74.43
Lower bound	80.36	79.94	74.68	71.41	84.97	84.32	85.09	85.68	81.28	80.34	80.81
Upper bound w/o BDA	85.89	83.85	80.73	84.56	87.59	90.45	89.54	90.81	85.94	87.42	86.68
Upper bound	85.59	84.11	80.23	83.55	88.40	90.63	90.00	91.50	86.06	87.45	86.75
Cutmix[39]	85.22	78.65	76.94	77.36	85.81	85.21	84.30	88.34	83.07	82.39	82.73

Mixup[54]	80.44	74.02	71.90	70.95	86.02	80.07	83.56	85.63	80.48	77.67	79.07
BigAug[13]	83.47	77.73	78.73	77.02	85.75	83.11	84.97	86.82	83.23	81.17	82.20
Manifold Mixup[38]	76.87	70.43	78.67	75.31	81.04	80.81	85.06	87.58	80.41	78.53	79.47
Dofe[9]	85.13	78.94	81.00	81.10	87.39	85.94	84.96	86.80	84.62	83.20	83.91
Dofe w/ wrong domain label	83.91	81.74	78.99	78.96	83.97	85.80	84.78	87.91	82.91	83.60	83.26
CDDSA[10]	83.46	82.52	78.74	74.44	85.77	86.28	86.28	85.26	83.56	82.13	82.84
CDDSA w/ wrong domain label	79.33	75.84	76.27	73.28	85.00	85.94	84.91	85.87	81.38	80.23	80.80
UniDDG w/o EMA	83.61	80.25	78.48	75.70	83.56	81.88	85.94	87.37	82.90	81.30	82.10
UniDDG w/o SA	84.14	81.71	79.62	76.47	86.85	84.51	86.95	88.11	84.39	82.70	83.55
UniDDG	85.54	82.69	80.07	76.93	87.16	87.92	86.93	88.22	84.93	83.94	84.43

Table 3 and Table 4 present the quantitative evaluation results of OC and OD segmentation in terms of Dice and ASSD, respectively, for the various DG methods. The inclusion of BDA played a pivotal role in these experiments, particularly when comparing the upper and lower bounds with and without BDA. The results clearly highlight the importance of BDA in improving model generalization. For the lower bound, the Dice score increased from 74.43% (without BDA) to 80.81% (with BDA), and the ASSD improved from 8.28 pixels to 4.52 pixels, indicating that enhancing the visual diversity of training data significantly aids in model generalization. However, when considering the upper bound, the improvement from 86.68% (without BDA) to 86.75% (with BDA) was marginal, suggesting that in settings where domain shifts are less severe, the contribution of BDA to improving generalization is limited. This finding emphasizes that while BDA provides essential benefits in more challenging domain generalization tasks, its impact is less pronounced when the domain shifts are relatively small. Therefore, these results validate the importance of BDA as a fundamental strategy for enhancing model robustness, while also pointing out that its effects are most substantial when domain shifts are more significant.

Table 4 Evaluation of ASSD (pixel) using diverse DG approaches on fundus image dataset from multiple source centers to a single target center

Method	Center1		Center2		Center3		Center4		Average		All
	OC	OD	OC	OD	OC	OD	OC	OD	OC	OD	
Lower bound w/o BDA	7.53	4.60	13.12	10.36	4.38	3.82	5.53	16.88	7.64	8.92	8.28
Lower bound	6.49	3.80	6.00	7.04	3.72	3.59	2.65	2.86	4.72	4.32	4.52
Upper bound w/o BDA	4.64	3.23	4.09	3.81	2.89	2.17	1.83	1.68	3.36	2.72	3.04
Upper bound	4.77	3.07	4.24	3.55	2.73	2.11	1.75	1.58	3.37	2.58	2.97
Cutmix[39]	5.13	3.84	6.06	4.70	3.19	3.12	2.72	2.14	4.27	3.45	3.86
Mixup[54]	6.35	4.54	12.64	10.90	3.59	4.12	3.13	2.54	6.42	5.53	5.97
BigAug[13]	5.51	3.91	4.48	4.51	3.38	3.52	2.66	2.34	4.01	3.57	3.79
Manifold Mixup[38]	7.57	4.96	4.82	4.68	4.21	4.20	2.63	2.13	4.81	3.99	4.40
Dofe[9]	4.83	4.52	4.03	3.68	2.91	2.90	2.46	2.29	3.56	3.35	3.45
Dofe w/ wrong domain label	5.22	4.22	4.62	4.45	3.56	2.94	3.60	2.17	4.25	3.44	3.85
CDDSA[10]	5.49	2.14	4.74	5.89	3.18	2.78	2.27	2.75	3.92	3.39	3.65
CDDSA w/ wrong domain label	6.78	3.50	5.37	5.64	3.67	3.37	2.62	3.06	4.61	3.89	4.25
UniDDG w/o EMA	5.41	3.78	6.13	5.16	4.08	5.24	3.00	3.81	4.66	4.50	4.58
UniDDG w/o SA	5.48	3.69	4.54	5.02	3.09	3.69	2.38	2.27	3.87	3.67	3.77
UniDDG	4.79	3.20	4.35	5.02	2.93	2.58	2.35	5.88	3.61	4.17	3.89

UniDDG consistently achieved the best performance, with an average Dice score of 84.43%, outperforming state-of-the-art DG methods such as CutMix (82.73%), Mixup (79.07%), BigAug (82.20%), Manifold Mixup (79.47%), Dofe (83.91%), and CDDSA (82.84%), which also significantly outperform the lower bound (80.81%). The improvement over Dofe, despite its strong performance, highlights the effectiveness of UniDDG in capturing and leveraging domain-invariant features while maintaining robust generalization. Regarding ASSD, UniDDG delivered an average of 3.89 pixels, indicating precise boundary delineation. Although Dofe achieved a slightly lower ASSD (3.45 pixels), its Dice score was noticeably inferior. This observation highlights the trade-off between boundary

precision and overall segmentation quality. Dice score, being a more holistic metric for segmentation quality, holds greater importance in practical applications, especially when global segmentation accuracy is prioritized.

Comparing UniDDG with other DG methods demonstrates its advantages. Techniques like Mixup and CutMix, which are effective in natural image domains, struggle to preserve the structural and spatial complexities of medical images. Methods such as BigAug and Manifold Mixup lack sufficient adaptability to domain-specific challenges in medical imaging. While Dofe’s domain-oriented feature embedding improves boundary precision, it falls short in achieving competitive Dice scores, reflecting its limitations in overall segmentation quality. CDDSA, which employs contrastive domain disentanglement and style augmentation, also shows limitations, with lower Dice scores and higher ASSD compared to UniDDG. UniDDG’s strong performance across both metrics highlights its robustness in multi-source-to-single-target scenarios, even under significant domain shifts. The framework effectively balances segmentation accuracy (Dice score) with boundary precision (ASSD), surpassing competing methods. Visual comparisons (Figure 6) further confirm that UniDDG achieves the largest overlap with the ground truth in the segmented regions, with fewer discrepancies in segmentation compared to other DG methods.

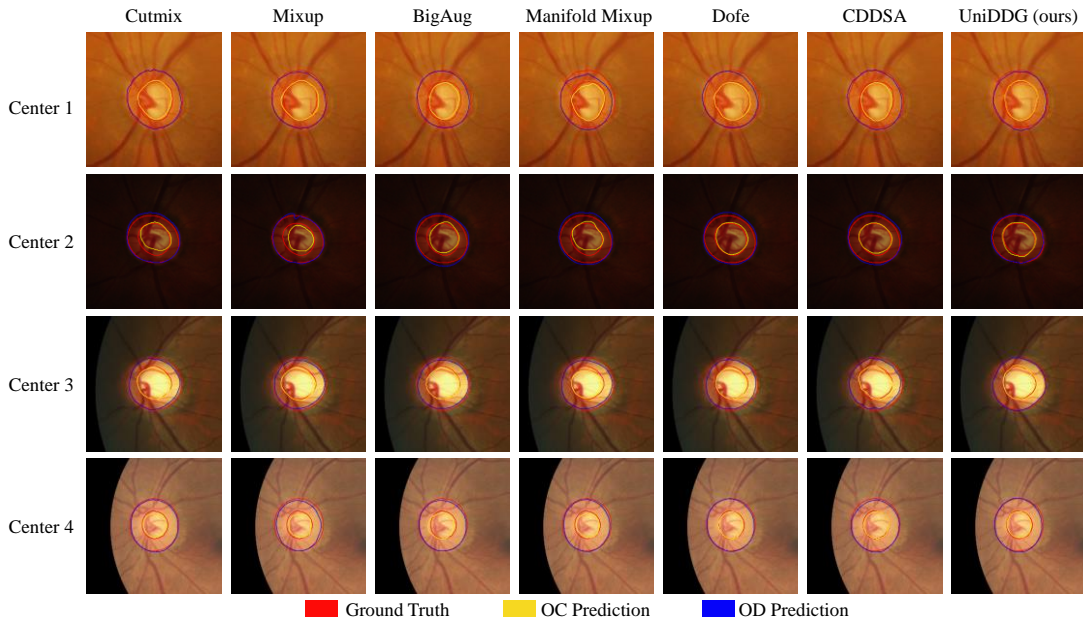


Figure 6 (Best viewed in color) Visualization of segmentation results using diverse DG approaches on fundus image dataset from multiple source centers to a single target center

(ii) Ablation studies: This section investigates the contributions of the EMA and SA modules to the performance of the UniDDG framework through ablation studies. To achieve this, we compare three model variants: UniDDG w/o EMA, UniDDG w/o SA, and the full UniDDG model. These variants were created by individually removing the EMA and SA modules, and their performance was evaluated quantitatively, as shown in Table 3 and Table 4.

The UniDDG w/o EMA variant, which excludes the expansion mask attention (EMA) module, shows a significant drop in performance. Specifically, the Dice score decreased from 84.43% in the full UniDDG model to 82.10%, while the Average Symmetric Surface Distance (ASSD) increased from 3.89

pixels to 4.58 pixels. These results underscore the importance of the EMA module in improving segmentation accuracy and preserving boundary details. To better understand this, Figure 7 provides visualizations of reconstructed images from a single batch during training for both the full UniDDG model and the UniDDG w/o EMA configuration. In the full UniDDG setting, the reconstructed images x'_i , $x'_{i \rightarrow j}$, and $x'_{i \rightarrow rd}$ successfully retain the complete structures of the optic disc, optic cup, and their surrounding regions, ensuring that critical anatomical features are preserved for effective segmentation.

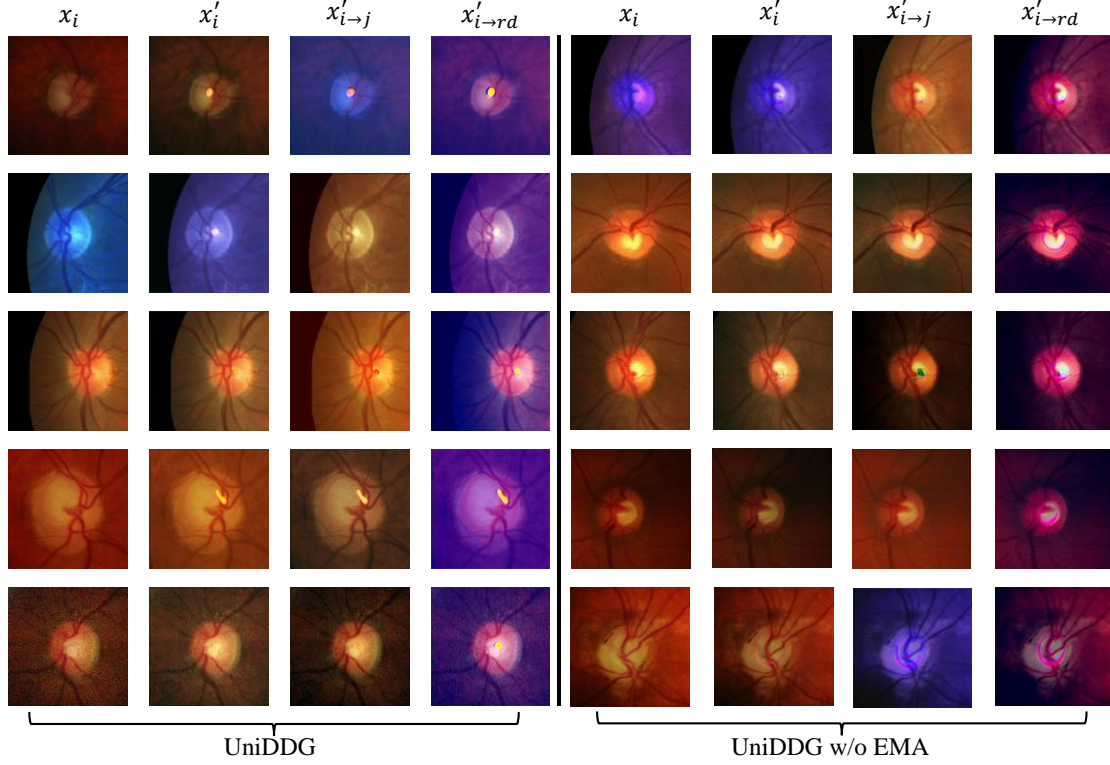


Figure 7 (Best viewed in color) Visualization of reconstructed images of one batch during training process (note this is the last batch in an epoch, so batch size is not the 8 mentioned earlier). x_i , x'_i , $x'_{i \rightarrow j}$, and $x'_{i \rightarrow rd}$ represent original image, reconstruction of original image, reconstructed image of exchanging styles within a batch, and reconstructed image with a random style

In contrast, the UniDDG w/o EMA configuration produces reconstructed images that exhibit prominent artificial contour lines around the boundaries of the optic disc and optic cup. These contour lines are introduced into the training process through the content encoder and segmentation head, significantly affecting the learning dynamics of the model. On one hand, these artificial contours may mislead the segmentation model into interpreting them as actual boundary features, resulting in inaccurate segmentations. On the other hand, even if these contours align with true boundaries, their artificial nature causes the model to rely excessively on them for boundary detection. This reliance undermines the model’s ability to generalize to real-world datasets where such contour lines are absent, leading to degraded performance. The removal of EMA thus results in noticeable declines in both quantitative metrics and qualitative reconstruction outcomes, emphasizing its critical role in segmentation accuracy and generalization.

For the UniDDG w/o SA variant, which excludes the style augmentation (SA) module, the results show a slight improvement in boundary precision, with the ASSD decreasing from 3.89 pixels to 3.77 pixels. However, the Dice score also decreases slightly, from 84.43% to 83.55%, indicating a minor

compromise in overall segmentation accuracy. The SA module introduces diverse style information during training (as shown as $x'_{i \rightarrow rd}$ in Figure 7), which enhances the model’s robustness to varying domain styles. While removing the SA module reduces variability in boundary precision, it slightly hampers the model’s ability to adapt to style changes across domains. This adaptability is critical for maintaining robust performance under diverse conditions, even if it comes at the cost of marginally reduced precision in boundary detection.

In summary, the ablation studies reveal that the EMA and SA modules contribute uniquely to the performance of the UniDDG model. The EMA module is essential for capturing fine boundary details and ensuring accurate segmentation, while the SA module enhances the model’s adaptability to style variations across domains. The removal of EMA leads to a significant decline in performance, whereas the removal of SA slightly reduces overall accuracy while improving boundary precision. Together, these modules complement each other in the full UniDDG model, enabling it to achieve both high segmentation accuracy and robustness to domain shifts.

4.3.2. Generalization within a single center

(i) Comparison with state-of-the-art DG methods: For evaluating the generalization performance of the proposed UniDDG framework within a single center, both the training and testing datasets are derived from the same center. We trained a U-Net [1] using standard Dice loss as the lower bound, which serves as the upper bound in the evaluation of generalization from multiple source centers to a single target center, as shown in Table 3 and Table 4. Consequently, the results of the upper bound and upper bound w/o BDA from these tables are directly used as the lower bound and lower bound w/o BDA for the experiments in this section. In comparison with state-of-the-art domain generalization (DG) methods, we focus on the methods most suitable for this scenario: UniDDG, Cutmix, Mixup, BigAug, and Manifold Mixup. Dofe and CDDSA, which were designed specifically for multi-source center scenarios, are not appropriate for this single-center experiment and, therefore, is excluded from this comparison.

Table 5 and Table 6 present the quantitative evaluation results for OC and OD segmentation in terms of Dice score and ASSD, respectively, comparing various domain generalization (DG) methods within a single-center scenario. The results demonstrate that the proposed UniDDG method outperforms the lower bound, as well as several state-of-the-art DG methods, confirming its superior generalization capability.

In the Dice score evaluation (Table 5), UniDDG achieved an average score of 88.91%, which is a significant improvement over the lower bound (86.75%). This indicates that UniDDG effectively improves generalization and achieves high-quality segmentation. Compared to other methods, UniDDG consistently performs better. For instance, Cutmix and Mixup achieved average Dice scores of 87.38% and 86.89%, respectively, while BigAug and Manifold Mixup achieved scores of 87.17% and 85.57%, respectively. These results highlight UniDDG’s ability to achieve more accurate segmentation than other methods that rely on data augmentation techniques.

Table 5 Evaluation of Dice Scores (%) using diverse DG approaches on fundus image dataset within a single center

Method	Center1		Center2		Center3		Center4		Average		
	OC	OD	OC	OD	OC	OD	OC	OD	OC	OD	All
Lower bound w/o BDA	85.89	83.85	80.73	84.56	87.59	90.45	89.54	90.81	85.94	87.42	86.68
Lower bound	85.59	84.11	80.23	83.55	88.40	90.63	90.00	91.50	86.06	87.45	86.75
Cutmix[39]	85.36	85.02	83.40	85.41	88.28	90.65	89.62	91.29	86.67	88.09	87.38
Mixup[54]	85.88	85.14	81.74	84.78	87.93	90.27	88.66	90.73	86.05	87.73	86.89
BigAug[13]	86.72	83.58	82.49	85.73	87.96	90.63	89.29	90.92	86.62	87.72	87.17
Manifold Mixup[38]	86.21	84.50	74.87	81.31	88.06	90.16	88.93	90.50	84.52	86.62	85.57
UniDDG w/o EMA	85.59	84.74	84.39	86.72	88.89	90.92	90.17	91.96	87.26	88.59	87.92

UniDDG w/o SA	88.64	87.20	84.89	87.48	88.50	89.56	90.34	92.08	88.09	89.08	88.59
UniDDG	89.01	87.27	84.89	87.42	88.95	91.03	90.66	92.03	88.38	89.44	88.91

For the ASSD evaluation (Table 6), UniDDG achieved an average of 2.52 pixels, outperforming the lower bound (2.97 pixels) and demonstrating better boundary delineation and precision. In comparison, Cutmix, Mixup, BigAug, and Manifold Mixup achieved average ASSD values of 2.76, 2.83, 2.76, and 3.17, respectively, indicating that UniDDG provides better boundary accuracy. These results further confirm that UniDDG excels in both segmentation accuracy (Dice score) and boundary precision (ASSD), surpassing the performance of other methods.

While data augmentation techniques such as Cutmix, Mixup, BigAug, and Manifold Mixup have been widely used to improve model generalization, their performance in this single-center scenario is relatively limited. This is likely due to the fact that domain shifts between the training and testing datasets are relatively small in this setting. Although domain shifts do exist (as indicated by the lower bound results), they are not as severe as in multi-center scenarios, and the performance improvement from these augmentation techniques is constrained. In contrast, UniDDG’s domain generalization approach, which leverages advanced techniques to address domain discrepancies, consistently outperforms these state-of-the-art augmentation-based methods.

Table 6 Evaluation of ASSD (pixel) using diverse DG approaches on fundus image dataset within a single center

Method	Center1		Center2		Center3		Center4		Average		
	OC	OD	OC	OD	OC	OD	OC	OD	OC	OD	All
Lower bound w/o BDA	4.64	3.23	4.09	3.81	2.89	2.17	1.83	1.68	3.36	2.72	3.04
Lower bound	4.77	3.07	4.24	3.55	2.73	2.11	1.75	1.58	3.37	2.58	2.97
Cutmix[39]	4.76	2.81	3.55	2.86	2.71	2.05	1.76	1.56	3.19	2.32	2.76
Mixup[54]	4.63	2.79	4.05	2.79	2.80	2.06	1.89	1.64	3.34	2.32	2.83
BigAug[13]	4.43	2.86	3.79	2.75	2.77	2.02	1.84	1.60	3.21	2.30	2.76
Manifold Mixup[38]	4.51	2.84	6.38	3.29	2.72	2.06	1.85	1.71	3.86	2.47	3.17
UniDDG w/o EMA	4.69	2.94	3.46	2.42	2.86	2.05	1.70	1.48	3.18	2.22	2.70
UniDDG w/o SA	3.71	2.35	3.32	2.38	2.73	3.19	1.70	1.45	2.86	2.34	2.60
UniDDG	3.57	2.52	3.46	2.85	2.57	2.00	1.64	1.57	2.81	2.23	2.52

(ii) Ablation studies: We also conducted ablation experiments similar to the previous section, where we systematically removed the EMA and SA modules from the UniDDG framework. The quantitative evaluation results are summarized in Table 5 and Table 6.

The results show that removing either module leads to a decrease in performance. Specifically, UniDDG w/o EMA exhibited a noticeable performance drop, with the Dice score decreasing from 88.91% to 87.92%, and the ASSD increasing from 2.52 pixels to 2.70 pixels. Similarly, UniDDG w/o SA also resulted in a slight decline in Dice score from 88.91% to 88.59%, and a slight decline in ASSD, increasing it from 2.52 pixels to 2.60 pixels.

These results highlight the importance and effectiveness of both modules: both EMA and SA play a crucial role in stabilizing training, enhancing segmentation accuracy, and improving the model’s ability to adapt to domain shifts. Removing either of these modules leads to a decline in performance, underscoring the synergistic effect of EMA and SA in the full UniDDG model.

4.4. Prostate MRI segmentation

4.4.1. Generalization from multiple source centers to a single target center

(i) Comparison with state-of-the-art DG methods: To further validate the effectiveness of the UniDDG framework for medical image segmentation, we conducted experiments on a prostate MRI

dataset, employing the same evaluation protocol as that used for the retinal fundus segmentation dataset (see section 4.3.1). The results from the prostate MRI dataset reaffirm the robustness and adaptability of UniDDG in addressing domain shifts in medical imaging tasks.

Table 7 and Table 8 present the comparison results for the prostate MRI segmentation. In the lower bound setup, domain shifts between the centers are significant, leading to a relatively larger gap in performance. On the other hand, in the upper bound setup, where training and testing data come from the same center, the domain shift is relatively smaller, resulting in higher performance. The results show that when basic data augmentation (BDA) is applied, the Dice scores and ASSD values improve significantly in the lower bound scenario, where domain shifts are more severe. However, the improvements are relatively small in the upper bound scenario, where the domain shifts are weaker. This trend mirrors the findings in retinal fundus image segmentation, where BDA has a significant impact in cases with substantial domain shifts and only a marginal effect when the domain shift is small.

Table 7 Evaluation of Dice Scores (%) using diverse DG approaches on prostate MRI dataset from multiple source centers to a single target center

Method	Center1	Center2	Center3	Center4	Center5	Average
Lower bound w/o BDA	84.43	74.19	80.41	74.52	83.40	79.39
Lower bound	85.17	83.36	83.78	78.01	84.28	82.92
Upper bound w/o BDA	88.08	86.02	86.59	83.00	77.47	84.23
Upper bound	88.00	88.53	89.61	81.74	78.45	85.27
Cutmix[39]	85.72	80.88	88.40	85.46	84.43	84.98
Mixup[54]	83.84	75.99	84.20	78.90	78.57	80.30
BigAug[13]	85.36	85.12	86.97	81.57	83.90	84.58
Manifold Mixup[38]	84.61	73.70	84.75	76.59	81.97	80.32
Dofe[9]	85.77	86.18	88.54	80.32	83.16	84.79
Dofe w/ wrong domain label	84.05	82.46	85.66	79.69	83.15	83.00
CDDSA[10]	85.22	82.27	87.10	81.99	80.90	83.50
CDDSA w/ wrong domain label	82.60	80.24	82.78	78.43	78.89	80.59
UniDDG w/o EMA	86.68	86.87	87.48	80.29	86.37	85.54
UniDDG w/o SA	87.22	85.59	87.64	81.09	86.43	85.59
UniDDG	87.65	88.01	89.16	83.70	86.30	86.96

As summarized in Table 7, the Dice scores (%) obtained across multiple centers demonstrate that UniDDG outperforms all baseline domain generalization (DG) methods, achieving the highest average Dice score of 86.96%. Compared to the best-performing baseline method, Cutmix, which achieved an average Dice score of 84.98%, UniDDG provides a significant improvement of +1.98%. This consistent performance across all five target centers highlights the effectiveness of UniDDG in maintaining segmentation accuracy across diverse domains.

Table 8 Evaluation of ASSD (pixel) using diverse DG approaches on prostate MRI dataset from multiple source centers to a single target center

Method	Center1	Center2	Center3	Center4	Center5	Average
Lower bound w/o BDA	3.95	6.58	6.21	6.26	2.65	5.13
Lower bound	3.29	3.86	4.92	3.89	2.48	3.69
Upper bound w/o BDA	2.62	4.03	3.50	2.94	4.25	3.47
Upper bound	3.56	3.95	2.18	7.43	3.04	4.03
Cutmix[39]	4.11	6.05	3.08	1.99	2.41	3.53
Mixup[54]	3.58	7.54	3.12	3.15	3.11	4.10
BigAug[13]	5.07	3.06	2.91	3.69	2.50	3.45
Manifold Mixup[38]	4.15	7.18	3.18	5.50	2.74	4.55
Dofe[9]	3.12	3.37	2.41	2.48	2.95	2.87
Dofe w/ wrong domain label	5.25	4.58	4.12	4.04	3.05	4.21
CDDSA[10]	4.57	5.29	4.43	2.12	4.78	4.24
CDDSA w/ wrong domain label	5.05	6.59	5.13	3.05	5.37	5.04
UniDDG w/o EMA	2.77	2.92	2.91	3.87	2.20	2.93
UniDDG w/o SA	2.66	3.12	3.17	6.16	2.16	3.46
UniDDG	2.63	4.20	2.65	2.88	2.14	2.90

In terms of boundary precision, Table 8 presents the average ASSD (in pixels) for different DG methods. While Dofe achieves the lowest average ASSD of 2.87 pixels, UniDDG closely follows with an ASSD of 2.90 pixels. It is worth noting, however, that the Dice score—a more comprehensive indicator of overall volumetric segmentation accuracy—is significantly higher for UniDDG compared to Dofe. This suggests that, despite the marginal difference in ASSD, UniDDG demonstrates a superior ability to ensure accurate segmentation across varying domain conditions, making it the more effective method overall. Visual comparisons (Figure 8) further confirm that UniDDG achieves the largest overlap with the ground truth in the segmented regions, with fewer discrepancies in segmentation compared to other DG methods.

These results on the prostate MRI dataset are consistent with the conclusions drawn from the retinal fundus segmentation experiments, further highlighting the generalizability and reliability of UniDDG. By achieving superior performance in both segmentation accuracy and boundary precision, UniDDG demonstrates its effectiveness as a robust framework for generalizing from multiple source centers to a single target center in medical image segmentation tasks, making it highly applicable to real-world clinical scenarios.

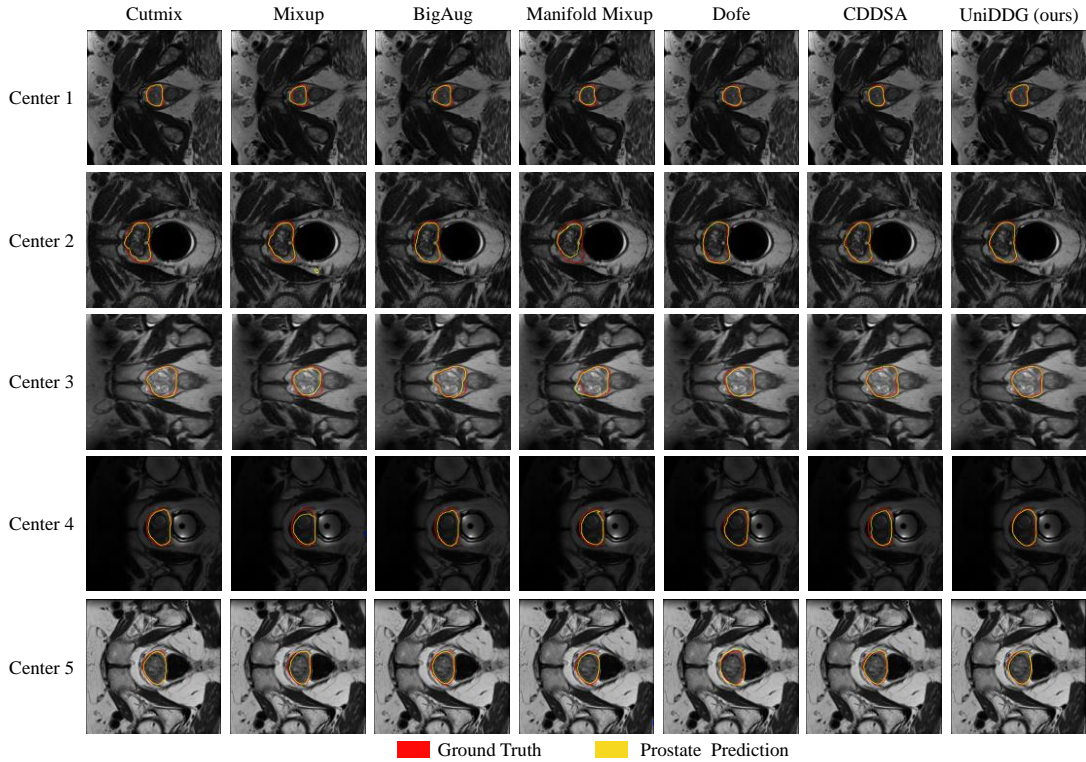


Figure 8 (Best viewed in color) Visualization of segmentation results using diverse DG approaches on prostate MRI dataset from multiple source centers to a single target center

(ii) Ablation studies: To investigate the contributions of different components in the UniDDG framework, we conducted ablation studies by removing the EMA and SA modules, similar to the previous section. The results from these experiments, summarized in Table 7 and Table 8, help us understand the role of each component in improving the generalization and segmentation performance of the model.

When the EMA module was removed (UniDDG w/o EMA), there was a noticeable drop in

performance. Specifically, the average Dice score decreased from 86.96% to 85.54%, a reduction of 1.42%, and the average ASSD increased from 2.90 pixels to 2.93 pixels. This indicates that the EMA module plays a crucial role in stabilizing the training process and ensuring more consistent performance across different target centers. The slight increase in boundary precision (ASSD) further emphasizes that the EMA module helps maintain segmentation accuracy and fine boundary delineation.

Similarly, removing the SA module (UniDDG w/o SA) also led to a performance decline, although the impact was less pronounced compared to the removal of the EMA module. The average Dice score decreased from 86.96% to 85.59%, and the average ASSD increased from 2.90 pixels to 3.46 pixels. The decrease in Dice score and the increase in ASSD suggest that the SA module plays a vital role in capturing long-range dependencies within the input images, which improves segmentation accuracy and boundary precision. This supports the notion that attention mechanisms help enhance model performance by focusing on relevant regions in the image.

4.4.2. Generalization within a single center

(i) Comparison with state-of-the-art DG methods: To investigate the performance of UniDDG in the context of a single target center, we conducted experiments using a prostate MRI dataset, following the same evaluation protocol as in the section 4.3.2. In this case, the generalization task involves training on data from a single center and testing on data from the same center, which is more representative of real-world clinical scenarios where data from a specific medical facility is used for model development.

Table 9 Evaluation of Dice Scores (%) using diverse DG approaches on prostate MRI dataset within a single center

Method	Center1	Center2	Center3	Center4	Center5	Average
Lower bound w/o BDA	88.08	86.02	86.59	83.00	77.47	84.23
Lower bound	88.00	88.53	89.61	81.74	78.45	85.27
Cutmix[39]	88.59	88.55	90.66	86.56	76.27	86.13
Mixup[54]	87.64	83.97	88.43	81.88	76.32	83.65
BigAug[13]	88.47	86.02	89.44	83.16	75.51	84.52
Manifold Mixup[38]	88.10	85.22	88.49	82.21	73.21	83.45
UniDDG w/o EMA	88.38	89.57	90.65	87.38	78.52	86.90
UniDDG w/o SA	88.66	90.21	90.72	88.17	81.07	87.77
UniDDG	89.09	91.36	90.93	89.23	82.20	88.56

As shown in Table 9 and Table 10, UniDDG consistently outperforms the other domain generalization (DG) methods in both Dice score and ASSD. Specifically, UniDDG achieves the highest average Dice score of 88.56%, surpassing the best-performing baseline method, Cutmix, by 2.43%. Additionally, in terms of boundary precision, UniDDG achieves the lowest average ASSD of 2.56 pixels, outperforming Cutmix (3.08 pixels) and all other methods. This indicates that UniDDG excels in both overall segmentation accuracy and fine boundary delineation, making it a highly effective framework for generalizing medical image segmentation tasks within a single center. The results further demonstrate UniDDG’s ability to maintain segmentation performance across different centers, showcasing its robustness in handling variations in medical imaging data.

Table 10 Evaluation of ASSD (pixel) using diverse DG approaches on prostate MRI dataset within a single center

Method	Center1	Center2	Center3	Center4	Center5	Average
Lower bound w/o BDA	2.62	4.03	3.50	2.94	4.25	3.47
Lower bound	3.56	3.95	2.18	7.43	3.04	4.03
Cutmix[39]	2.54	2.75	2.12	2.24	5.77	3.08
Mixup[54]	2.73	4.42	2.23	3.26	6.16	3.76
BigAug[13]	3.43	4.03	2.13	3.02	8.30	4.18
Manifold Mixup[38]	3.35	4.05	2.40	3.10	6.52	3.88
UniDDG w/o EMA	3.48	2.56	2.13	1.94	3.95	2.81
UniDDG w/o SA	3.46	2.45	2.00	4.35	3.03	3.06

UniDDG	3.21	2.16	1.92	2.13	3.39	2.56
--------	-------------	-------------	-------------	------	------	-------------

ii) Ablation studies: To better understand the individual contributions of each component in the UniDDG framework, we conducted ablation studies by removing the EMA and SA modules. These components are designed to improve the model's focus on critical regions during segmentation and enhance its robustness to style variations, respectively. The results of these experiments are summarized in Table 9 and Table 10.

When the EMA module was removed (UniDDG w/o EMA), the performance showed a noticeable decline. Specifically, the average Dice score decreased from 88.56% to 86.90%, and the average ASSD increased from 2.56 pixels to 2.81 pixels. This drop in performance demonstrates that EMA plays a significant role in enhancing boundary precision by guiding the model to focus on critical regions, particularly the boundaries of the target object. The slight increase in ASSD further confirms that EMA helps in maintaining accurate boundary delineation, ensuring that the model captures fine details of the segmentation.

Similarly, when the SA module was removed (UniDDG w/o SA), the performance also decreased, albeit to a lesser extent. The average Dice score dropped from 88.56% to 87.77%, and the average ASSD increased from 2.56 pixels to 3.06 pixels. This indicates that the SA module contributes to the model's robustness against image style variations. By augmenting the content encoder and segmenter with random style codes, the SA module ensures that the model is less sensitive to changes in image style, thereby maintaining consistent segmentation performance. The slight drop in performance when SA is removed underscores the importance of this module in making the model more adaptable to varying image styles.

The results from these ablation studies indicate that both EMA and SA significantly contribute to the overall performance of UniDDG. EMA enhances the model's ability to focus on key regions for precise segmentation, particularly near object boundaries, while SA improves robustness to style variations. The performance drops observed when these modules are removed highlight their essential roles in improving segmentation accuracy and boundary precision, especially in the context of prostate MRI segmentation.

4.5. Multi-source domain generalization under misassigned explicit domain labels

In DG tasks, methods like Dofe and CDDSA typically rely heavily on explicit domain labels during training to define source domains for model adaptation. These approaches assume that domain labels are correctly assigned and used during the training phase. However, in real-world applications, domain labels may be misassigned or even unavailable, which can significantly compromise model performance. In contrast, our proposed UniDDG model does not rely on explicit domain labels based on the "one image as one domain" (OIOD) hypothesis. It treats each image as an individual domain, with all source domain data mixed together during training without explicit label assignments. This randomization reduces the dependency on domain labels and enhances the model's robustness to domain shifts.

To evaluate the degree of dependency on explicit domain labels, we conducted an experiment where we shuffled domain labels across multiple source centers. Specifically, we mixed the data from different centers into a single image pool and then randomly reassigned domain labels (as shown in Figure 9). After shuffling the labels, each "new domain" contained the same amount of data as the original, but with incorrect label assignments. We then used t-SNE to visualize the feature distributions of the training data before and after label shuffling (Figure 10).

Before shuffling, the feature distributions of images from each center were well-separated, with distinct clusters formed by each center’s data. However, after shuffling, the feature distributions became mixed, making it difficult to distinguish data belonging to different centers based solely on their feature space. This illustrates that the misassignment of domain labels causes the feature distributions to lose their original structure.

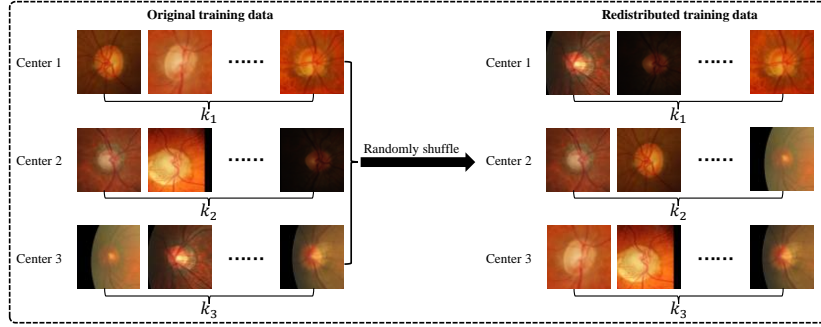


Figure 9 (Best viewed in color) Illustration of shuffling domain labels of multi-source central data

We then trained Dofe and CDDSA on the shuffled data using the incorrect domain labels and evaluated their generalization performance on a new target center. The results are presented in Table 3, Table 4, Table 7, and Table 8. Table 3 and Table 4 involve the segmentation of the optic cup and optic disc from retinal images, while Table 7 and Table 8 focus on prostate MRI image segmentation tasks. The results for Dofe and CDDSA with shuffled domain labels are labeled as Dofe w/ wrong domain label and CDDSA w/ wrong domain label. As shown in these tables, both methods exhibited significant performance degradation when domain labels were incorrect.

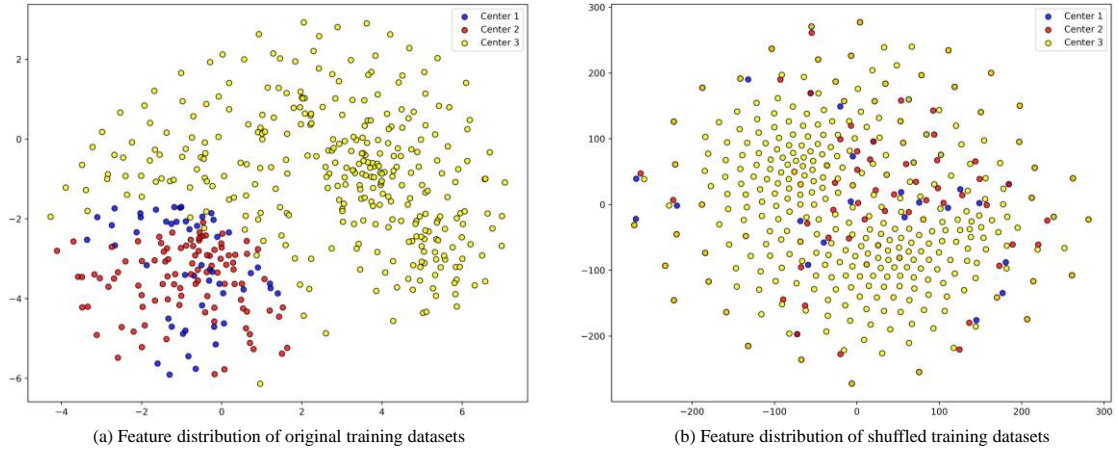


Figure 10 (Best viewed in color) t-SNE visualization of VGG16 features of retinal fundus images from original and shuffled training datasets for OC/OD segmentation

For example, in Table 3 (Dice scores for retinal image segmentation), Dofe’s performance dropped from 83.91% to 83.26% with shuffled labels, while CDDSA showed a more substantial decrease from 82.84% to 80.80%. In Table 4 (ASSD for retinal image segmentation), Dofe’s ASSD increased from 3.45 to 3.85, while CDDSA’s ASSD rose sharply from 3.65 to 4.25. Similarly, in Table 7 and Table 8, where the segmentation task involves prostate MRI images, the performance of Dofe and CDDSA significantly worsened when domain labels were shuffled. This confirms that both Dofe and CDDSA rely heavily on

explicit domain labels during training. The performance drop was especially pronounced in CDDSA, suggesting that this method is more sensitive to misassigned domain labels compared to Dofe.

The stronger dependency of CDDSA on domain labels can be attributed to the "Domain Style Contrastive Learning" trick incorporated in the method. This trick requires domain labels to effectively separate the features of different domains. The method forces the model to push the features of different domains apart while pulling features from the same domain closer together in the feature space. This contrastive learning approach is heavily reliant on explicit domain labels, making CDDSA more sensitive to label misassignment than Dofe.

In contrast, our UniDDG method does not rely on explicit domain labels and is therefore relatively unaffected by domain label misassignments. Since the training process of UniDDG deliberately removes the dependence on domain labels, it avoids the performance drop observed in Dofe and CDDSA when domain labels are shuffled. This highlights the robustness of UniDDG's domain-agnostic approach, which performs well even when domain labels are incorrectly assigned, making it better suited for real-world scenarios where domain labels may be unreliable or unavailable.

5. Conclusion

In this paper, we have proposed a novel perspective on domain generalization for medical image segmentation, which challenges the conventional practice of grouping images from the same center or scanner as a single domain. We introduce the "one image as one domain" (OIOD) hypothesis, which treats each image as an individual domain, acknowledging the inherent variability within and across centers. This perspective enables more flexible and robust generalization, as it accounts for both inter-center and intra-center domain shifts that are often overlooked in traditional domain generalization methods.

Building on the OIOD hypothesis, we present the UniDDG framework, a unified disentanglement-based domain generalization approach that is capable of handling both single-source and multi-source domain generalization without requiring explicit domain labels. Unlike existing disentanglement methods that rely on complex GAN architectures, UniDDG simplifies the training process by decoupling content representation and style code through operations such as exchange, recombination, and reconstruction. This decoupling does not increase computational complexity, and the network's parameter count remains fixed regardless of the number of source domains. Furthermore, UniDDG incorporates expansion mask attention (EMA) to preserve boundaries during reconstruction and style augmentation (SA) to simulate diverse image styles, enhancing the model's robustness to domain shifts.

Through extensive experiments on both multi-source and single-source medical image segmentation tasks, including optic disc and cup segmentation, as well as prostate segmentation, our approach demonstrates superior performance compared to existing state-of-the-art methods. The results show that UniDDG outperforms traditional domain generalization techniques in both segmentation accuracy and adaptability to diverse clinical settings.

In conclusion, the proposed UniDDG framework, grounded in the OIOD hypothesis, offers a powerful and flexible solution to the challenges of domain generalization in medical image segmentation. By redefining the concept of a domain and eliminating the need for explicit domain labels, we believe our approach paves the way for more robust and scalable models that can better generalize to unseen data across diverse healthcare environments.

Declaration of competing interest

The authors declare that there are no conflicts of interest regarding the publication of this paper.

CRediT authorship contribution statement

Jin Hong: Conceptualization; Data curation; Formal analysis; Investigation; Methodology; Software; Validation; Visualization; Resources; Funding acquisition; Project administration; Supervision; Writing-review & editing; Writing-original draft. **Bo Liu:** Validation; Visualization, Software, Writing-review & editing. **Guoli Long:** Data curation, Writing-review & editing.

Acknowledgements

This work was supported in part by the National Natural Science Foundation of China (62466033), in part by the Jiangxi Provincial Natural Science Foundation (20242BAB20070).

References

1. Ronneberger, O., P. Fischer, and T. Brox. *U-net: Convolutional networks for biomedical image segmentation*. in *International Conference on Medical image computing and computer-assisted intervention*. 2015. Springer.
2. Isensee, F., P.F. Jaeger, S.A. Kohl, J. Petersen, and K.H. Maier-Hein, *nnU-Net: a self-configuring method for deep learning-based biomedical image segmentation*. *Nature methods*, 2021. **18**(2): p. 203-211.
3. Zhou, Z., M.M.R. Siddiquee, N. Tajbakhsh, and J. Liang, *Unet++: Redesigning skip connections to exploit multiscale features in image segmentation*. *IEEE transactions on medical imaging*, 2019. **39**(6): p. 1856-1867.
4. Hong, J., S.C.-H. Yu, and W. Chen, *Unsupervised domain adaptation for cross-modality liver segmentation via joint adversarial learning and self-learning*. *Applied Soft Computing*, 2022. **121**: p. 108729.
5. Hong, J., Y.-D. Zhang, and W. Chen, *Source-free unsupervised domain adaptation for cross-modality abdominal multi-organ segmentation*. *Knowledge-Based Systems*, 2022. **250**: p. 109155.
6. Li, S., S. Zhao, Y. Zhang, J. Hong, and W. Chen, *Source-free unsupervised adaptive segmentation for knee joint MRI*. *Biomedical Signal Processing and Control*, 2024. **92**: p. 106028.
7. Guan, H. and M. Liu, *Domain adaptation for medical image analysis: a survey*. *IEEE Transactions on Biomedical Engineering*, 2021. **69**(3): p. 1173-1185.
8. Chen, C., Q. Dou, H. Chen, J. Qin, and P.A. Heng, *Unsupervised bidirectional cross-modality adaptation via deeply synergistic image and feature alignment for medical image segmentation*. *IEEE transactions on medical imaging*, 2020. **39**(7): p. 2494-2505.
9. Wang, S., L. Yu, K. Li, X. Yang, C.-W. Fu, and P.-A. Heng, *Dofe: Domain-oriented feature embedding for generalizable fundus image segmentation on unseen datasets*. *IEEE Transactions on Medical Imaging*, 2020. **39**(12): p. 4237-4248.
10. Gu, R., G. Wang, J. Lu, J. Zhang, W. Lei, Y. Chen, W. Liao, S. Zhang, K. Li, and D.N. Metaxas, *CDDSA: Contrastive domain disentanglement and style augmentation for generalizable medical image segmentation*. *Medical Image Analysis*, 2023. **89**: p. 102904.
11. Zhou, K., Z. Liu, Y. Qiao, T. Xiang, and C.C. Loy, *Domain generalization: A survey*. *IEEE Transactions on Pattern Analysis and Machine Intelligence*, 2022. **45**(4): p. 4396-4415.
12. Su, Z., K. Yao, X. Yang, K. Huang, Q. Wang, and J. Sun. *Rethinking data augmentation for single-source domain generalization in medical image segmentation*. in *Proceedings of the AAAI Conference on Artificial Intelligence*. 2023.
13. Zhang, L., X. Wang, D. Yang, T. Sanford, S. Harmon, B. Turkbey, B.J. Wood, H. Roth, A. Myronenko, and D. Xu, *Generalizing deep learning for medical image segmentation to unseen domains via deep stacked transformation*. *IEEE transactions on medical imaging*, 2020. **39**(7): p. 2531-2540.
14. Gu, R., J. Zhang, R. Huang, W. Lei, G. Wang, and S. Zhang. *Domain composition and attention for unseen-domain generalizable medical image segmentation*. in *Medical Image Computing and Computer Assisted Intervention–MICCAI*

- 2021: 24th International Conference, Strasbourg, France, September 27–October 1, 2021, Proceedings, Part III 24. 2021. Springer.
15. Tzeng, E., J. Hoffman, N. Zhang, K. Saenko, and T. Darrell, *Deep domain confusion: Maximizing for domain invariance*. arXiv preprint arXiv:1412.3474, 2014.
 16. Sun, B. and K. Saenko. *Deep coral: Correlation alignment for deep domain adaptation*. in *European conference on computer vision*. 2016. Springer.
 17. Hoffman, J., D. Wang, F. Yu, and T. Darrell, *Fcns in the wild: Pixel-level adversarial and constraint-based adaptation*. arXiv preprint arXiv:1612.02649, 2016.
 18. Chen, Y.-H., W.-Y. Chen, Y.-T. Chen, B.-C. Tsai, Y.-C. Frank Wang, and M. Sun. *No more discrimination: Cross city adaptation of road scene segmenters*. in *Proceedings of the IEEE International Conference on Computer Vision*. 2017.
 19. Ganin, Y., E. Ustinova, H. Ajakan, P. Germain, H. Larochelle, F. Laviolette, M. Marchand, and V. Lempitsky, *Domain-adversarial training of neural networks*. *The journal of machine learning research*, 2016. **17**(1): p. 2096-2030.
 20. Tzeng, E., J. Hoffman, K. Saenko, and T. Darrell. *Adversarial discriminative domain adaptation*. in *Proceedings of the IEEE conference on computer vision and pattern recognition*. 2017.
 21. Vu, T.-H., H. Jain, M. Bucher, M. Cord, and P. Pérez. *Advent: Adversarial entropy minimization for domain adaptation in semantic segmentation*. in *Proceedings of the IEEE/CVF Conference on Computer Vision and Pattern Recognition*. 2019.
 22. Kamnitsas, K., C. Baumgartner, C. Ledig, V. Newcombe, J. Simpson, A. Kane, D. Menon, A. Nori, A. Criminisi, and D. Rueckert. *Unsupervised domain adaptation in brain lesion segmentation with adversarial networks*. in *International conference on information processing in medical imaging*. 2017. Springer.
 23. Dou, Q., C. Ouyang, C. Chen, H. Chen, and P.-A. Heng. *Unsupervised cross-modality domain adaptation of convnets for biomedical image segmentations with adversarial loss*. in *Proceedings of the 27th International Joint Conference on Artificial Intelligence*. 2018.
 24. Bousmalis, K., N. Silberman, D. Dohan, D. Erhan, and D. Krishnan. *Unsupervised pixel-level domain adaptation with generative adversarial networks*. in *Proceedings of the IEEE conference on computer vision and pattern recognition*. 2017.
 25. Zhu, J.-Y., T. Park, P. Isola, and A.A. Efros. *Unpaired image-to-image translation using cycle-consistent adversarial networks*. in *Proceedings of the IEEE international conference on computer vision*. 2017.
 26. Chang, W.-L., H.-P. Wang, W.-H. Peng, and W.-C. Chiu. *All about structure: Adapting structural information across domains for boosting semantic segmentation*. in *Proceedings of the IEEE/CVF Conference on Computer Vision and Pattern Recognition*. 2019.
 27. Yang, J., N.C. Dvornek, F. Zhang, J. Chapiro, M. Lin, and J.S. Duncan. *Unsupervised domain adaptation via disentangled representations: Application to cross-modality liver segmentation*. in *International Conference on Medical Image Computing and Computer-Assisted Intervention*. 2019. Springer.
 28. Zou, Y., Z. Yu, B. Kumar, and J. Wang. *Unsupervised domain adaptation for semantic segmentation via class-balanced self-training*. in *Proceedings of the European conference on computer vision (ECCV)*. 2018.
 29. French, G., M. Mackiewicz, and M. Fisher, *Self-ensembling for visual domain adaptation*. arXiv preprint arXiv:1706.05208, 2017.
 30. Perone, C.S., P. Ballester, R.C. Barros, and J. Cohen-Adad, *Unsupervised domain adaptation for medical imaging segmentation with self-ensembling*. *NeuroImage*, 2019. **194**: p. 1-11.
 31. Novosad, P., V. Fonov, and D.L. Collins, *Unsupervised domain adaptation for the automated segmentation of neuroanatomy in MRI: a deep learning approach*. *bioRxiv*, 2019: p. 845537.
 32. Hoffman, J., E. Tzeng, T. Park, J.-Y. Zhu, P. Isola, K. Saenko, A. Efros, and T. Darrell. *Cycada: Cycle-consistent adversarial domain adaptation*. in *International conference on machine learning*. 2018. PMLR.

33. Wu, Z., X. Han, Y.-L. Lin, M.G. Uzunbas, T. Goldstein, S.N. Lim, and L.S. Davis. *Dcan: Dual channel-wise alignment networks for unsupervised scene adaptation*. in *Proceedings of the European Conference on Computer Vision (ECCV)*. 2018.
34. Zhao, S., B. Li, X. Yue, Y. Gu, P. Xu, R. Hu, H. Chai, and K. Keutzer. *Multi-source domain adaptation for semantic segmentation*. *Advances in Neural Information Processing Systems*, 2019. **32**.
35. He, J., X. Jia, S. Chen, and J. Liu. *Multi-source domain adaptation with collaborative learning for semantic segmentation*. in *Proceedings of the IEEE/CVF Conference on Computer Vision and Pattern Recognition*. 2021.
36. Heusel, M., H. Ramsauer, T. Unterthiner, B. Nessler, and S. Hochreiter. *Gans trained by a two time-scale update rule converge to a local nash equilibrium*. *Advances in neural information processing systems*, 2017. **30**.
37. Wu, F. and X. Zhuang. *Unsupervised Domain Adaptation With Variational Approximation for Cardiac Segmentation*. *IEEE Transactions on Medical Imaging*, 2021. **40**(12): p. 3555-3567.
38. Verma, V., A. Lamb, C. Beckham, A. Najafi, I. Mitliagkas, D. Lopez-Paz, and Y. Bengio. *Manifold mixup: Better representations by interpolating hidden states*. in *International conference on machine learning*. 2019. PMLR.
39. Yun, S., D. Han, S.J. Oh, S. Chun, J. Choe, and Y. Yoo. *Cutmix: Regularization strategy to train strong classifiers with localizable features*. in *Proceedings of the IEEE/CVF international conference on computer vision*. 2019.
40. Peng, D., Y. Lei, M. Hayat, Y. Guo, and W. Li. *Semantic-aware domain generalized segmentation*. in *Proceedings of the IEEE/CVF conference on computer vision and pattern recognition*. 2022.
41. Choi, S., S. Jung, H. Yun, J.T. Kim, S. Kim, and J. Choo. *Robustnet: Improving domain generalization in urban-scene segmentation via instance selective whitening*. in *Proceedings of the IEEE/CVF conference on computer vision and pattern recognition*. 2021.
42. Hu, S., Z. Liao, J. Zhang, and Y. Xia. *Domain and Content Adaptive Convolution Based Multi-Source Domain Generalization for Medical Image Segmentation*. *IEEE Transactions on Medical Imaging*, 2023. **42**(1): p. 233-244.
43. Liu, Q., C. Chen, J. Qin, Q. Dou, and P.-A. Heng. *Feddg: Federated domain generalization on medical image segmentation via episodic learning in continuous frequency space*. in *Proceedings of the IEEE/CVF conference on computer vision and pattern recognition*. 2021.
44. Chatsias, A., T. Joyce, G. Papanastasiou, S. Semple, M. Williams, D.E. Newby, R. Dharmakumar, and S.A. Tsaftaris. *Disentangled representation learning in cardiac image analysis*. *Medical Image Analysis*, 2019. **58**: p. 101535.
45. Milletari, F., N. Navab, and S.-A. Ahmadi. *V-net: Fully convolutional neural networks for volumetric medical image segmentation*. in *2016 fourth international conference on 3D vision (3DV)*. 2016. IEEE.
46. Kingma, D.P. *Auto-encoding variational bayes*. arXiv preprint arXiv:1312.6114, 2013.
47. Huang, X., M.-Y. Liu, S. Belongie, and J. Kautz. *Multimodal unsupervised image-to-image translation*. in *Proceedings of the European conference on computer vision (ECCV)*. 2018.
48. Sivaswamy, J., S. Krishnadas, A. Chakravarty, G. Joshi, and A.S. Tabish. *A comprehensive retinal image dataset for the assessment of glaucoma from the optic nerve head analysis*. *JSM Biomedical Imaging Data Papers*, 2015. **2**(1): p. 1004.
49. Fumero, F., S. Alayón, J.L. Sanchez, J. Sigut, and M. Gonzalez-Hernandez. *RIM-ONE: An open retinal image database for optic nerve evaluation*. in *2011 24th international symposium on computer-based medical systems (CBMS)*. 2011. IEEE.
50. Orlando, J.I., H. Fu, J.B. Breda, K. Van Keer, D.R. Bathula, A. Diaz-Pinto, R. Fang, P.-A. Heng, J. Kim, and J. Lee. *Refuge challenge: A unified framework for evaluating automated methods for glaucoma assessment from fundus photographs*. *Medical image analysis*, 2020. **59**: p. 101570.
51. Bloch, B.N., A. Madabhushi, H. Huisman, J. Freymann, J. Kirby, M. Grauer, A. Enquobahrie, C. Jaffe, L. Clarke, and K. Farahani. *NCI-ISBI 2013 Challenge: Automated Segmentation of Prostate Structures (ISBI-MR-Prostate-2013)*. 2015, The Cancer Imaging Archive.
52. Lemaître, G., R. Martí, J. Freixenet, J.C. Vilanova, P.M. Walker, and F. Meriaudeau. *Computer-aided detection and*

- diagnosis for prostate cancer based on mono and multi-parametric MRI: a review*. Computers in biology and medicine, 2015. **60**: p. 8-31.
53. Litjens, G., R. Toth, W. Van De Ven, C. Hoeks, S. Kerkstra, B. Van Ginneken, G. Vincent, G. Guillard, N. Birbeck, and J. Zhang, *Evaluation of prostate segmentation algorithms for MRI: the PROMISE12 challenge*. Medical image analysis, 2014. **18**(2): p. 359-373.
54. Zhang, H., *mixup: Beyond empirical risk minimization*. arXiv preprint arXiv:1710.09412, 2017.